

Observation and Reanalysis Derived Relationships Between Cloud and Land Surface Fluxes Across Cumulus and Stratiform Coupling Over the Southern Great Plains

Tianning Su^{1,2}, Zhanqing Li¹, Yunyan Zhang², Youtong Zheng^{3,4}, Haipeng Zhang¹

¹AOSC & ESSIC, University of Maryland at College Park, Maryland, 20740, USA

²Lawrence Livermore National Laboratory, Livermore, CA, USA

³Department of Earth and Atmospheric Science, University of Houston, Houston, TX, USA

⁴Institute for Climate and Atmospheric Science, University of Houston, Houston, TX,
USA

*Corresponding authors: zhanqing@umd.edu; su10@llnl.gov

Key Points:

- This study develops a diagnostic approach for untangling cloud-land relationships across distinct cloud coupling regimes.
 - Field observations are utilized to assess performances of reanalysis data in representing cloud-land interaction across different regimes.
 - Findings emphasize the importance of differentiating cloud coupling regimes in observational and modeling studies of boundary layer clouds.

Keywords: clouds; land surface; sensible heat; reanalysis data; cloud-land coupling

29 **Abstract.** Understanding interactions between low clouds and land surface fluxes is
30 critical to comprehending Earth's energy balance, yet their relationships remain elusive,
31 with discrepancies between observations and modeling. Leveraging long-term field
32 observations over the Southern Great Plains, this investigation revealed that cloud-land
33 interactions are closely connected to cloud-land coupling regimes. Observational
34 evidence supports a dual-mode interaction: coupled stratiform clouds predominate in
35 low sensible heat scenarios, while coupled cumulus clouds dominate in high sensible
36 heat scenarios. Reanalysis datasets, MERRA-2 and ERA-5, obscure this dichotomy
37 owing to a shortfall in representing boundary layer clouds, especially in capturing the
38 initiation of coupled cumulus in high sensible heat scenarios. ERA-5 demonstrates a
39 relatively closer alignment with observational data, particularly in capturing
40 relationships between cloud frequency and latent heat, markedly outperforming
41 MERRA-2. Our study underscores the necessity of distinguishing different cloud
42 coupling regimes is necessary to the understanding of their interactions, crucial for
43 advancing land-atmosphere interactions.

44

45 1 Introduction

46 Low clouds are key players in Earth's climate, influencing radiative balance and
47 climate feedback loops. Continental low-level clouds are influenced by the land surface
48 via processes occurring within the planetary boundary layer (PBL) (Betts, 2009;
49 Teixeira and Hogan, 2002; Golaz et al., 2002; Berg and Kassianov, 2008; Yang et al.,
50 2019; Guo et al., 2019; Zhang et al., 2017; Fast et al., 2019a). These clouds often emerge
51 within the PBL's entrainment zone under convective conditions, yet their coupling with
52 the land surface is complex and presents challenges in accurate determination and
53 analysis (Su et al., 2022). Thus, a comprehensive examination of how terrestrial
54 processes affect cloud evolution is warranted to understand the coupling of low-level
55 clouds with the land surface (Bretherton et al., 2007; Moeng et al., 1996; Su et al., 2023;
56 Xian et al., 2023; Zheng et al., 2021).

57 Extensive research has been carried out to investigate cloud-land interactions,
58 highlighting the important roles of land surface heterogeneity, evaporative fraction, and

59 soil moisture (Yue et al. 2017; Tang et al., 2019; Qian et al., 2023). Specifically, multiple
60 studies have documented how land surface heterogeneity impacts the formation of
61 shallow convection and development (Rieck et al. 2014; Xiao et al. 2018; Lee et al.
62 2019). Fast et al. (2019b) and Tao et al. (2019) have elucidated the strength of land-
63 atmosphere interactions and their important roles in modulating convective cloud
64 formation and evolution. As the majority of these studies have focused on local
65 convection or cumulus, the wide range of cloud types and their interactions with the
66 land surface present a complex and multifaceted challenge (Sakaguchi et al., 2022; Poll
67 et al., 2022; Tao et al., 2021). It is essential to delve into these characteristics and dissect
68 the cloud-land relationships across different regimes to achieve a more detailed
69 understanding of these interactions.

70 Cloud variables in reanalysis data have also been extensively utilized in numerous
71 studies (Su et al., 2013; Cesana et al., 2015), and have undergone detailed evaluations
72 for the vertical structure and spatial variations (Dolinar et al., 2016; Free et al., 2016;
73 Liu and Key, 2016). Several studies have reported the underestimation of low-level
74 cloud fraction in popular reanalysis datasets, such as the European Centre for Medium-
75 Range Weather Forecasts' fifth-generation global reanalysis (ERA-5), across different
76 regions (Miao et al., 2019; Peng et al., 2019; Danso et al., 2019). Besides, reanalysis
77 datasets face significant challenges in accurately representing the complex interactions
78 between low clouds and the land surface (Tao et al., 2021; Wang et al., 2023; Betts et
79 al., 2006). A gap exists in specifically assessing how these datasets capture cloud-land-
80 surface coupling, particularly under stratiform regimes. Consequently, the effectiveness
81 of reanalysis products in representing the relationships between clouds and land surface
82 fluxes across different coupling regimes warrants further investigation.

83 Our study addresses two primary objectives: firstly, to develop a diagnostic
84 approach for untangling cloud-land relationships across distinct cloud coupling regimes;
85 and secondly, to evaluate the performance of prevailing reanalysis datasets in
86 representing these relationships across different cloud regimes. Utilizing field
87 observations over the Atmospheric Radiation Measurement (ARM) Southern Great
88 Plains (SGP) site, we examine the interactions between low clouds and land surface

89 fluxes under different cloud regimes, including coupled stratiform, coupled cumulus,
90 and decoupled clouds. This analysis sheds light on the different interactions within these
91 regimes and also highlights the discrepancies in reanalysis datasets.

92

93 **2 Data and Method**

94 *2.1 Observational and reanalysis dataset*

95 The ARM program, funded by the U.S. Department of Energy, has been operational
96 at the SGP site in Oklahoma (36.607°N , 97.488°W) for decades. This study uses an
97 extensive array of data from the SGP observatory from 1998 to 2020 to investigate the
98 relationships between cloud characteristics and surface fluxes. These observational
99 datasets include the Active Remote Sensing of Clouds (ARSCL, Clothiaux et al. 2000,
100 2001; Kollias et al. 2020), thermodynamic profiles from radiosonde, in-situ surface flux
101 measurements, and meteorological data recorded at the surface (Cook, 2018; Xie et al.,
102 2010).

103 We further use reanalysis datasets from the ERA-5 (Hersbach et al., 2020) and
104 Modern-Era Retrospective analysis for Research and Applications Version 2 (MERRA-
105 2, Gelaro et al., 2017). As the state-of-art reanalysis data, the ERA-5 is produced by the
106 Integrated Forecasting System (IFS) and a data assimilation system at a fine spatial
107 resolution of $0.25^{\circ} \times 0.25^{\circ}$. Meanwhile, the MERRA-2 offers atmospheric and land
108 information at a resolution of $0.5^{\circ} \times 0.625^{\circ}$ (Randles et al., 2017). An important
109 difference between the ERA-5 and MERRA-2 is the cloud parameterization: ERA-5
110 uses a prognostic cloud scheme (Tiedtke 1993) that accounts for the impacts from
111 previous time steps whereas MERRA-2 uses a diagnostic cloud scheme. The
112 procurement, processing, and quality assurance steps for observational and reanalysis
113 datasets are further detailed in Supporting Information Section 1.

114

115 *2.2 Identification of cloud coupling regimes*

116 Su et al. (2022) developed a micropulse lidar-based approach to discern the cloud-
117 land coupling by accounting for the vertical coherence and temporal continuity of PBL
118 height (PBLH). Clouds are defined as coupled when the turbulence originating from

119 the surface is able to reach the cloud base, thereby influencing its evolution, resulting
120 in a turbulence-facilitated linkage among surface fluxes, PBL, and the cloud. Utilizing
121 PBLH, the cloud base, and surface-based LCL calculations in accordance with Romps
122 (2017), we differentiate between coupled and decoupled low-level clouds. The method
123 for calculating PBLH is detailed in Su et al. (2020) which has been used to develop a
124 PBLH climatological dataset at the central facilities of SGP. Coupled clouds are
125 identified by the alignment of cloud base height (CBH) with the lidar-detected PBL top
126 and LCL within a defined range, while decoupled clouds, which form independently of
127 surface-driven updrafts, are indicated by a lack of this alignment.

128 Following the determination of cloud-land coupling, we exclude precipitation
129 events exceeding 0.1 mm h^{-1} to prevent distortion in lidar signals and surface flux
130 measurements. The study focuses on data from 09:00 to 15:00 Local Time (LT) to avoid
131 the late afternoon period when the PBL typically begins to decay. We exclude the
132 coexistence of coupled and decoupled low clouds during this period and further
133 implement a classification into cumulus and stratiform categories among coupled cloud
134 days. For coupled cumulus, two conditions are implemented in line with practices from
135 previous studies (Zhang and Klein 2010, 2013; Lareau et al., 2018): (1) cloud
136 formations must emerge after sunrise without low clouds at 08:00 LT to make sure that
137 clouds are driven by local convection; (2) there is absence of overcast clouds. Coupled
138 stratiform clouds are characterized by prolonged overcast clouds, which last more than
139 3 hours. Overcast low-level clouds have a cloud fraction of more than 90% based on
140 ASRSL data.

141 Figure S1 showcases these cloud regimes, with coupled cumulus manifesting as
142 discrete cellular formations in satellite imagery, and coupled stratiform clouds
143 displaying broad, extensive coverage starting from the previous night. Meanwhile,
144 decoupled clouds are distinguished by their separation from surface-driven PBL
145 activity. Applying this methodological framework has led to the identification of 631
146 days marked by coupled cumulus and 470 days with coupled stratiform clouds across
147 all seasons. In addition, we have distinguished 578 days with decoupled clouds across
148 two decades, excluding instances with mixed coupled and decoupled low clouds.

149 Compared to the conventional approaches focused on identifying the specific types of
150 clouds (e.g., cumulus or stratocumulus), our approach delineates different cloud-land
151 coupling regimes, encompassing both coupled/decoupled states and cumulus/stratiform
152 regimes. This enables a comprehensive analysis of cloud-land interactions, examining
153 these relationships through the perspective of cloud-land coupling.

154

155 **3 Results**

156 *3.1 Overall relationship between cloud occurrence frequency and surface fluxes*

157 Our investigation begins by exploring the connection between the frequency of low
158 cloud occurrences and surface sensible and latent heat fluxes. The evaluation criterion
159 for low cloud occurrence is based on cloud fraction where the maximum value between
160 the surface and 700 hPa exceeds a 1% threshold. This study employs hourly mean
161 values for analysis, with hourly low cloud occurrence categorized as 0 or 1. The cloud
162 frequency is further calculated by dividing the sum by the total number of hours
163 analyzed. This analysis incorporates data from both observational sources and the
164 reanalysis datasets of ERA-5 and MERRA-2, as detailed in Figure 1. For the overall
165 relationship, the same precipitation filter of 0.1 mm h^{-1} has been applied to the
166 observation, ERA-5, and MERRA-2. Observational findings depicted in Figures 1a-b
167 showcase a dual-mode interaction: cloud frequencies initially diminish at lower
168 sensible heat levels and subsequently augment with an increase in sensible heat.

169 When extending the analysis to reanalysis datasets, different responses of cloud to
170 surface fluxes emerge (Figures 1c-f). The correlation between surface fluxes observed
171 and those within reanalysis datasets is presented in Figure S2. While ERA-5 partially
172 captures the essence of the observed cloud-land relationships, particularly for latent
173 heat, it still exhibits discrepancies in cloud frequency concerning sensible heat. ERA-5
174 data reflects a trend of decreasing cloud frequency with rising sensible heat, compared
175 to the dual-mode interaction in the observations.

176 MERRA-2's response, however, is notably different; it presents a systematic
177 underestimation of cloud occurrences across all surface flux ranges. MERRA-2's cloud
178 representation deviates markedly, reinforcing concerns about its sensitivity to the

179 processes that drive cloud development under varying thermal conditions. Figure S3
180 accentuates this point by showing that both reanalysis datasets, especially MERRA-2,
181 consistently underrepresent the average low cloud fractions across the spectrum of
182 sensible and latent heat fluxes compared to observational data.

183

184 *3.2 Characteristics for different cloud regimes*

185 To elucidate the complex relationship between cloud presence and terrestrial
186 influences, Figure 2 presents the changes of cloud occurrence frequency relative to
187 surface sensible heat, stratified by specific cloud regimes. By excluding days where low
188 cloud regimes intermingle, we isolate the distinct behavioral signatures of each regime
189 among days with coupled/decoupled scenarios and clear-sky. In the juxtaposition of
190 reanalysis datasets against field observations, we examine the variation in cloud
191 frequency under different levels of sensible heat in Figure 2. For comparison, these
192 regimes of days are classified solely based on observational data and the relationships
193 are calculated from observation and reanalysis data for the same samples.

194 Coupled stratiform clouds are characterized by their extensive coverage and cloud
195 shading effects, predominating under low sensible heat conditions. As a result, there is
196 a notable decrease in sensible heat concurrent with the increase in cloud frequency, as
197 illustrated in Figures 2a-c. These clouds are associated with a well-mixed and unstable
198 sub-cloud layer, indicative of a dynamic exchange of heat and moisture with the
199 underlying surface, as depicted in Figure S4. The presence of widespread overcasting,
200 often concurrent with lower sensible heat, reinforces the persistence of stratiform clouds
201 by mitigating the drying effects of entrainment.

202 In the realm of coupled cumulus, an increase in sensible heat is linked to enhanced
203 cloud formation, as surface heating intensifies convective activity within the PBL.
204 During days when these clouds are present, ERA-5 data tend to underestimate the
205 frequency of locally generated convection under high sensible heat scenarios, as
206 reflected in Figure 2d-e. MERRA-2 demonstrates a significant deviation from observed
207 patterns, consistently missing a large fraction of low clouds (Figure 2f). Decoupled
208 clouds exhibit a more complex relationship with surface sensible heat (Figure 2g-i).

209 Although they do not interact directly with PBL thermodynamics, they exert a cloud
210 shading effect, leading to a suppression of surface sensible heat.

211 Figure 3 shows the relationships between cloud and latent heat. In analogy with the
212 trends observed for sensible heat, coupled stratiform clouds demonstrate a diminishing
213 frequency with increasing latent heat. On the other hand, coupled cumulus clouds tend
214 to occur more frequently as latent heat increases, indicative of a conducive environment
215 for cloud coupling, possibly through mechanisms such as lowering the LCL alongside
216 PBL growth. This highlights that moderate to strong latent heat particularly promotes
217 cloud formation coupling. To address the gap between grid and point data, we employed
218 surface fluxes gridded to a spatial resolution of $0.25^\circ \times 0.25^\circ$ for analyzing the cloud-
219 land relationships, revealing that the patterns of these relationships exhibit similarity
220 across both the gridded and point flux measurements (Figures S5 and Figure S6). In
221 addition, stratiform cloud frequency generally increases with the evaporative fraction,
222 emphasizing latent heat's role in their formation, while both ERA-5 and MERRA-2
223 inaccurately depict a decline in cloud frequency across evaporative fraction ranges and
224 also fail to accurately represent cumulus formation at lower evaporative fraction values,
225 which are primarily driven by sensible heat (Figure S7).

226 The diurnal variation in cloud fraction across the different regimes is further
227 illustrated in Figure 4, which underscores the notable biases present in reanalysis
228 datasets. MERRA-2 notably underestimates low-level cloud fractions. Despite a similar
229 pattern, ERA-5 struggles to represent local cumulus convection and decoupled cloud
230 scenarios with insufficient cloud fraction. Such underrepresentation of boundary layer
231 clouds culminates in a generalized underestimation of low clouds within both MERRA-
232 and ERA-5 (Figure S8). The underestimation in the low cloud fraction can also lead
233 to a weak surface cooling effect in reanalysis data.

234 Our results are related to prior studies that highlight diurnal biases in convection
235 over the central United States, particularly the challenges in accurately capturing local
236 convection and the insufficient triggering of cumulus, as detailed in studies by Tao et
237 al. (2021, 2023). Their studies also noted the shortfall in triggering shallow cumulus
238 clouds, contributing to the biases in convection patterns.

239

240 *3.3 Meteorological triggers for cloud formation across regimes*

241 Cloud development across various coupling regimes is linked to essential
242 meteorological factors, particularly atmospheric instability and humidity, as indicated
243 by PBLH and surface relative humidity (RH_{sfc}). Figure 5a presents the coupling-
244 decoupling difference, calculated as the difference between the frequencies of coupled
245 and decoupled clouds, and examines its correlations with changes in PBLH and RH_{sfc} .
246 Their relationships are also influenced by sensible heat marked in the grey-scale dots
247 showing the connections between PBLH and RH_{sfc} under an array of sensible heat
248 conditions. Figure 5b indicates the corresponding variations in the frequency of low
249 clouds under different values of PBLH and RH_{sfc} .

250 Distinct domains emerge within the coupled cloud zone: more coupled stratiform
251 clouds are prevalent in environments under higher RH_{sfc} and lower PBLH, typically
252 associated with lower sensible heat conditions. Conversely, coupled cumulus clouds
253 flourish under opposite conditions (i.e., lower RH_{sfc} and higher PBLH) suggestive of
254 higher sensible heat and strong convection. Decoupled clouds, inferred from their
255 negative coupling-decoupling differences, tend to occur towards lower PBLH across a
256 broader RH spectrum, indicating their formation is less contingent on surface-induced
257 convective processes. From low to high sensible heat, cloud regimes transit from
258 coupled stratiform to coupled cumulus clouds.

259 Figures 5c-d present comparative analyses of the frequency of clouds vis-à-vis
260 PBLH and RH_{sfc} , extracted from reanalysis datasets. Notably, both the occurrence and
261 fraction of clouds are misrepresented in MERRA-2. While the ERA-5 clouds generally
262 bear closer resemblance to the observed clouds, but still differ considerably in the
263 occurrences of both coupled stratiform clouds and coupled cumulus. The
264 underrepresentation of cumulus by the reanalysis stems from inadequate PBL
265 development under high sensible heat scenarios (Figure 5c-d). Meanwhile, the RH is
266 notably lower for the low sensible heat scenarios, which are linked with stratiform
267 clouds. The systematic underestimation in RH can contribute to the overall
268 underestimation of both cumulus and stratiform clouds, as illustrated in Figure S9,

269 further hindering the triggering of coupled clouds. These findings underscore the
270 critical need for enhancing the accuracy of surface flux and humidity representation in
271 reanalysis datasets, alongside refining the parametrization of their effects on convection.

272

273 **4. Discussion and Conclusions**

274 In this study, we dissect the complex relationships between low clouds and surface
275 fluxes over the Southern Great Plains, with a particular focus on cloud-land coupling
276 regimes. Building on previous studies that are primarily focused on cloud-land
277 interactions within shallow cumulus, we demonstrate that both the cumulus and
278 stratiform regimes represent distinct yet interconnected modes of cloud-land coupling.
279 Consequently, we explore a bifurcated interaction pattern within the framework of
280 cloud-land coupling, identifying that stratiform coupling prevails in low sensible heat
281 conditions, while cumulus coupling becomes the leading regime in high sensible heat
282 scenarios. Together, these findings portray the full paradigm of the coupling between
283 cloud and land surface, occurring under various conditions. It follows from analyses of
284 observations that meteorological conditions such as PBLH and RH are instrumental in
285 cloud formation across different regimes, with transitions from stratiform to cumulus
286 regimes leading to the overall pattern of cloud-land relationships.

287 Reanalysis datasets do not sufficiently capture the observed bifurcated interaction
288 pattern and present a damped decline pattern in the cloud-land relationship. MERRA-2
289 consistently underestimates cloud frequency across various cloud regimes, with a
290 particular shortfall in capturing the occurrence of coupled cumulus. ERA-5 generally
291 exhibits a commendable correlation with observational data, notably in the context of
292 latent heat interactions. However, ERA-5 still shows discrepancies, especially with the
293 frequency and initiation of coupled cumulus. Additionally, both reanalysis datasets fail
294 to represent decoupled clouds accurately, as these clouds' formation mechanisms appear
295 disconnected from local PBL processes, leading to notable differences in cloud fraction
296 estimates when compared to observational data.

297 This assessment of different cloud regimes underscores the significance of cloud
298 coupling in analyzing cloud-land interactions. The initiation of convection in coupled

299 cumulus is closely tied to surface processes on a sub-grid scale (Tian et al., 2022). As
300 these cloud regimes respond to climate change, misrepresentation of these cloud
301 dynamics within climate models could lead to uncertainties in predictions of climate
302 sensitivity, as posited by Schneider et al. (2019). The emergence of global storm-
303 resolving models with kilometer-scale resolutions, as detailed in Satoh et al. (2005),
304 Caldwell et al. (2021) and Hohenegger et al. (2023), may offer great potential for
305 addressing these complex modeling challenges in cloud-land interactions.

306

307 **Acknowledgements:** This work is supported in part by grants from the U.S.
308 Department of Energy (DE-SC0022919), the National Science Foundation
309 (AGS2126098), and NASA (80NSSC21K1980). Y. Zheng is supported by the DOE
310 Early Career Grant (DE-SC0024185). Y. Zhang is supported by the DOE Atmospheric
311 System Research (ASR) Science Focus Area (SFA) THREAD project. Work at LLNL
312 is performed under the auspices of the U.S. DOE by Lawrence Livermore National
313 Laboratory under Contract DE-AC52-07NA27344.

314

315 **Data Availability Statement:** ARM radiosonde data, surface fluxes, and cloud masks
316 are available online (ARM user facility. 1994). The identification for different cloud
317 regimes for the study period is publicly available (Su, 2023). The data of planetary
318 boundary layer are archived as an ARM product (Su and Li, 2023). Climate Data Store
319 offers the ERA-5 reanalysis data (Hersbach et al. 2023). MERRA-2 reanalysis data can
320 be downloaded online (GMAO, 2015).

321

322 **References**

- 323 Atmospheric Radiation Measurement (ARM) user facility. (1994). ARM Best Estimate
324 Data Products (ARMBEATM). Southern Great Plains (SGP) Central Facility,
325 Lamont, OK (C1). Compiled by C. Xiao and X. Shaocheng. [Dataset] ARM Data
326 Center. <http://dx.doi.org/10.5439/1333748>.
- 327 Berg, L. K., and Kassianov, E.I. (2008): Temporal variability of fair-weather cumulus
328 statistics at the ACRF SGP site. J. Climate, 21(13), 3344–3358.
- 329 Betts, A.K. (2009). Land-surface-atmosphere coupling in observations and models.

- 330 Journal of Advances in Modeling Earth Systems, 1(3).
- 331 Betts, A.K., Ball, J.H., Barr, A.G., Black, T.A., McCaughey, J.H. and Viterbo, P., 2006.
332 Assessing land-surface-atmosphere coupling in the ERA-40 reanalysis with boreal
333 forest data. *Agricultural and Forest Meteorology*, 140(1-4), pp.365-382.
- 334 Bretherton, C. S., Blossey, P. N., and Uchida, J. (2007): Cloud droplet sedimentation,
335 entrainment efficiency, and subtropical stratocumulus albedo. *Geophys. Res. Lett.*,
336 34(3), L03813.
- 337 Caldwell, P.M., Terai, C.R., Hillman, B., Keen, N.D., Bogenschutz, P., Lin, W.,
338 Beydoun, H., Taylor, M., Bertagna, L., Bradley, A.M. and Clevenger, T.C., 2021.
339 Convection-permitting simulations with the E3SM global atmosphere model.
340 *Journal of Advances in Modeling Earth Systems*, 13(11), p.e2021MS002544.
- 341 Cesana, G., Waliser, D.E., Jiang, X. and Li, J.L., 2015. Multimodel evaluation of cloud
342 phase transition using satellite and reanalysis data. *Journal of Geophysical Research: Atmospheres*, 120(15), pp.7871-7892.
- 344 Clothiaux, E.E., Ackerman, T.P., Mace, G.G., Moran, K.P., Marchand, R.T., Miller,
345 M.A. and Martner, B.E., 2000. Objective determination of cloud heights and radar
346 reflectivities using a combination of active remote sensors at the ARM CART sites.
347 *Journal of Applied Meteorology and Climatology*, 39(5), pp.645-665.
- 348 Clothiaux, E.E., Miller, M.A., Perez, R.C., Turner, D.D., Moran, K.P., Martner, B.E.,
349 Ackerman, T.P., Mace, G.G., Marchand, R.T., Widener, K.B. and Rodriguez, D.J.,
350 2001. The ARM millimeter wave cloud radars (MMCRs) and the active remote
351 sensing of clouds (ARSCL) value added product (VAP) (No. DOE/SC-ARM/VAP-
352 002.1). DOE Office of Science Atmospheric Radiation Measurement (ARM)
353 Program (United States).
- 354 Cook, D.R., 2018. Energy balance bowen ratio station (EBBR) instrument handbook
355 (No. DOE/SC-ARM/TR-037). DOE Office of Science Atmospheric Radiation
356 Measurement (ARM) Program (United States).
- 357 Danso, D.K., Anquetin, S., Diedhiou, A., Lavaysse, C., Kobe, A. and Touré, N.D.E.,
358 2019. Spatio-temporal variability of cloud cover types in West Africa with satellite-
359 based and reanalysis data. *Quarterly Journal of the Royal Meteorological Society*,
360 145(725), pp.3715-3731.
- 361 Dolinar, E.K., Dong, X. and Xi, B., 2016. Evaluation and intercomparison of clouds,
362 precipitation, and radiation budgets in recent reanalyses using satellite-surface
363 observations. *Climate Dynamics*, 46, pp.2123-2144.
- 364 Fast, J.D., Berg, L.K., Alexander, L., Bell, D., D'Ambro, E., Hubbe, J., Kuang, C., Liu,
365 J., Long, C., Matthews, A. and Mei, F., 2019b. Overview of the HI-SCALE field
366 campaign: A new perspective on shallow convective clouds. *Bulletin of the
367 American Meteorological Society*, 100(5), pp.821-840.
- 368 Fast, J.D., Berg, L.K., Feng, Z., Mei, F., Newsom, R., Sakaguchi, K. and Xiao, H.,

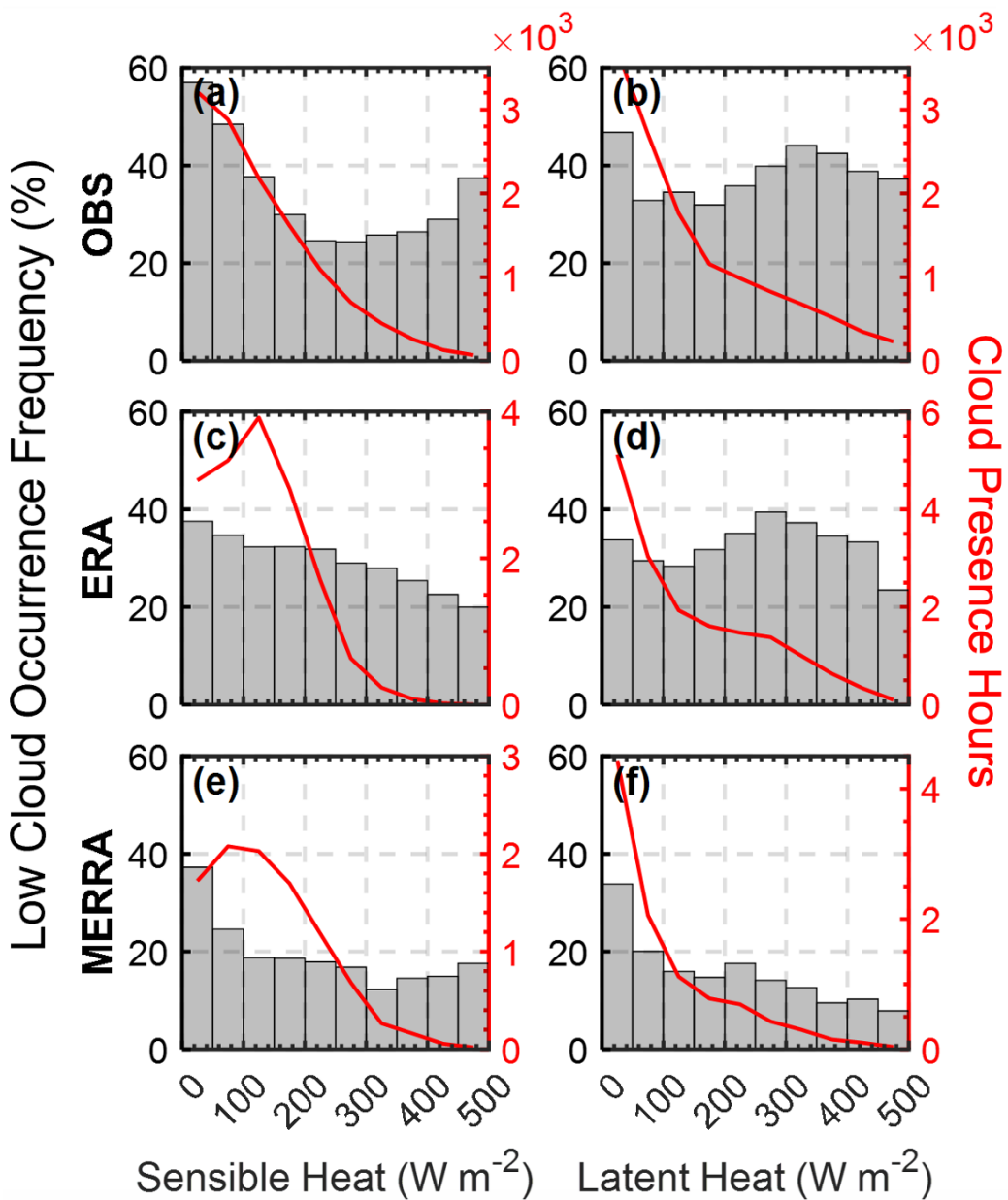
- 369 2019a. The impact of variable land-atmosphere coupling on convective cloud
370 populations observed during the 2016 HI-SCALE field campaign. *Journal of*
371 *Advances in Modeling Earth Systems*, 11(8), pp.2629-2654.
- 372 Free, M., Sun, B. and Yoo, H.L., 2016. Comparison between total cloud cover in four
373 reanalysis products and cloud measured by visual observations at US weather
374 stations. *Journal of Climate*, 29(6), pp.2015-2021.
- 375 Gelaro, R., McCarty, W., Suárez, M.J., Todling, R., Molod, A., Takacs, L., Randles,
376 C.A., Darmenov, A., Bosilovich, M.G., Reichle, R. and Wargan, K., 2017. The
377 modern-era retrospective analysis for research and applications, version 2
378 (MERRA-2). *Journal of climate*, 30(14), pp.5419-5454.
- 379 Global Modeling and Assimilation Office (GMAO) (2015), MERRA-2
380 tavg1_2d_rad_Nx: 2d,1-Hourly,Time-Averaged,Single-
381 Level,Assimilation,Radiation Diagnostics V5.12.4, Greenbelt, MD, USA [Dataset].
382 Goddard Earth Sciences Data and Information Services Center (GES DISC),
383 <https://doi.org/10.5067/Q9QMY5PBNV1T>.
- 384 Golaz, J.C., Larson, V.E. and Cotton, W.R. (2002). A PDF-based model for boundary
385 layer clouds. Part I: Method and model description. *Journal of the atmospheric*
386 *sciences*, 59(24), pp.3540-3551.
- 387 Guo, J., Su, T., Chen, D., Wang, J., Li, Z., Lv, Y., ... & Zhai, P. (2019). Declining
388 summertime local-scale precipitation frequency over China and the United States,
389 1981–2012: The disparate roles of aerosols. *Geophysical Research Letters*, 46(22),
390 13281-13289.
- 391 Hersbach, H., Bell, B., Berrisford, P., Biavati, G., Horányi, A., Muñoz Sabater, J.,
392 Nicolas, J., Peubey, C., Radu, R., Rozum, I., Schepers, D., Simmons, A., Soci, C.,
393 Dee, D., Thépaut, J-N. (2023): ERA5 hourly data on pressure levels from 1940 to
394 present. [Dataset] Copernicus Climate Change Service (C3S) Climate Data Store
395 (CDS), DOI: [10.24381/cds.bd0915c6](https://doi.org/10.24381/cds.bd0915c6).
- 396 Hersbach, H., Bell, B., Berrisford, P., Hirahara, S., Horányi, A., Muñoz-Sabater, J.,
397 Nicolas, J., Peubey, C., Radu, R., Schepers, D. and Simmons, A., 2020. The ERA5
398 global reanalysis. *Quarterly Journal of the Royal Meteorological Society*, 146(730),
399 pp.1999-2049.
- 400 Hohenegger, C., Korn, P., Linardakis, L., Redler, R., Schnur, R., Adamidis, P., Bao, J.,
401 Bastin, S., Behravesh, M., Bergemann, M. and Biercamp, J., 2023. ICON-Sapphire:
402 simulating the components of the Earth system and their interactions at kilometer
403 and subkilometer scales. *Geoscientific Model Development*, 16(2), pp.779-811.
- 404 Kollias, P., Bharadwaj, N., Clothiaux, E.E., Lamer, K., Oue, M., Hardin, J., Isom, B.,
405 Lindenmaier, I., Mathews, A., Luke, E.P. and Giangrande, S.E., 2020. The ARM
406 radar network: At the leading edge of cloud and precipitation observations. *Bulletin*
407 *of the American Meteorological Society*, 101(5), pp.E588-E607.

- 408 Lareau, N.P., Zhang, Y. and Klein, S.A. (2018). Observed boundary layer controls on
409 shallow cumulus at the ARM Southern Great Plains site. *Journal of the Atmospheric*
410 *Sciences*, 75(7), pp.2235-2255.
- 411 Lee, J.M., Zhang, Y. and Klein, S.A., 2019. The effect of land surface heterogeneity and
412 background wind on shallow cumulus clouds and the transition to deeper
413 convection. *Journal of the Atmospheric Sciences*, 76(2), pp.401-419.
- 414 Liu, Y. and Key, J.R., 2016. Assessment of Arctic cloud cover anomalies in atmospheric
415 reanalysis products using satellite data. *Journal of Climate*, 29(17), pp.6065-6083.
- 416 Miao, H., Wang, X., Liu, Y. and Wu, G., 2019. An evaluation of cloud vertical structure
417 in three reanalyses against CloudSat/cloud-aerosol lidar and infrared pathfinder
418 satellite observations. *Atmospheric Science Letters*, 20(7), p.e906.
- 419 Moeng, C.H., Cotton, W.R., Bretherton, C., Chlond, A., Khairoutdinov, M., Krueger,
420 S., Lewellen, W.S., MacVean, M.K., Pasquier, J.R.M., Rand, H.A. and Siebesma,
421 A.P. (1996). Simulation of a stratocumulus-topped planetary boundary layer:
422 Intercomparison among different numerical codes. *Bulletin of the American*
423 *Meteorological Society*, 77(2), pp.261-278.
- 424 Peng, X., She, J., Zhang, S., Tan, J. and Li, Y., 2019. Evaluation of multi-reanalysis
425 solar radiation products using global surface observations. *Atmosphere*, 10(2), p.42.
- 426 Poll, S., Shrestha, P. and Simmer, C. (2022). Grid resolution dependency of land surface
427 heterogeneity effects on boundary-layer structure. *Quarterly Journal of the Royal*
428 *Meteorological Society*, 148(742), pp.141-158.
- 429 Poll, S., Shrestha, P. and Simmer, C., 2022. Grid resolution dependency of land surface
430 heterogeneity effects on boundary-layer structure. *Quarterly Journal of the Royal*
431 *Meteorological Society*, 148(742), pp.141-158.
- 432 Qian, Y., Guo, Z., Larson, V.E., Leung, L.R., Lin, W., Ma, P.L., Wan, H., Wang, H.,
433 Xiao, H., Xie, S. and Yang, B., 2023. Region and cloud regime dependence of
434 parametric sensitivity in E3SM atmosphere model. *Climate Dynamics*, pp.1-17.
- 435 Randles, C.A., Da Silva, A.M., Buchard, V., Colarco, P.R., Darmenov, A., Govindaraju,
436 R., Smirnov, A., Holben, B., Ferrare, R., Hair, J. and Shinozuka, Y., 2017. The
437 MERRA-2 aerosol reanalysis, 1980 onward. Part I: System description and data
438 assimilation evaluation. *Journal of climate*, 30(17), pp.6823-6850.
- 439 Rieck, M., Hohenegger, C. and van Heerwaarden, C.C., 2014. The influence of land
440 surface heterogeneities on cloud size development. *Monthly Weather Review*,
441 142(10), pp.3830-3846.
- 442 Romps, D.M. (2017). Exact expression for the lifting condensation level. *Journal of the*
443 *Atmospheric Sciences*, 74(12), pp.3891-3900.
- 444 Sakaguchi, K., Berg, L.K., Chen, J., Fast, J., Newsom, R., Tai, S.L., Yang, Z., Gustafson
445 Jr, W.I., Gaudet, B.J., Huang, M. and Pekour, M., 2022. Determining spatial scales

- 446 of soil moisture—Cloud coupling pathways using semi-idealized simulations.
447 Journal of Geophysical Research: Atmospheres, 127(2), p.e2021JD035282.
- 448 Satoh, M., Tomita, H., Miura, H., Iga, S., and Nasuno, T, 2005. Development of a global
449 cloud resolving model – a multi-scale structure of tropical convections, J. Earth
450 Simulator, 3, 11–19.
- 451 Schneider, T., Kaul, C.M. and Pressel, K.G., 2019. Possible climate transitions from
452 breakup of stratocumulus decks under greenhouse warming. Nature Geoscience,
453 12(3), pp.163-167.
- 454 Su, H., Jiang, J.H., Zhai, C., Perun, V.S., Shen, J.T., Del Genio, A., Nazarenko, L.S.,
455 Donner, L.J., Horowitz, L., Seman, C. and Morcrette, C. (2013). Diagnosis of
456 regime-dependent cloud simulation errors in CMIP5 models using “A-Train”
457 satellite observations and reanalysis data. Journal of Geophysical Research:
458 Atmospheres, 118(7), pp.2762-2780.
- 459 Su, T. and Li, Z. (2023). Planetary Boundary Layer Height (PBLH) over SGP from
460 1998 to 2023. No. ARM0791. [Dataset] Atmospheric Radiation Measurement
461 (ARM) Archive;United States. <https://doi.org/10.5439/2007149>.
- 462 Su, T. (2023). Cloud Regime Identification over the SGP [Dataset]. Zenodo.
463 <https://doi.org/10.5281/zenodo.10437096>.
- 464 Su, T., Li, Z. and Zheng, Y. (2023). Cloud-Surface Coupling Alters the Morning
465 Transition From Stable to Unstable Boundary Layer. Geophysical Research Letters,
466 50(5), p.e2022GL102256.
- 467 Su, T., Li, Z., and Kahn, R. (2020): A new method to retrieve the diurnal variability of
468 planetary boundary layer height from lidar under different thermodynamic stability
469 conditions. Remote Sens. Environ., 237, 111519.
- 470 Su, T., Zheng, Y., and Li, Z. (2022). Methodology to determine the coupling of
471 continental clouds with surface and boundary layer height under cloudy conditions
472 from lidar and meteorological data. Atmospheric Chemistry and Physics, 22(2),
473 1453-1466.
- 474 Tang, S., Xie, S., Zhang, M., Tang, Q., Zhang, Y., Klein, S.A., Cook, D.R. and Sullivan,
475 R.C., 2019. Differences in eddy-correlation and energy-balance surface turbulent
476 heat flux measurements and their impacts on the large-scale forcing fields at the
477 ARM SGP site. Journal of Geophysical Research: Atmospheres, 124(6), pp.3301-
478 3318.
- 479 Tao, C., Xie, S., Ma, H.Y., Bechtold, P., Cui, Z., Vaillancourt, P.A., Choi, S.T., Wei, J.,
480 Wu, W.Y., Zhang, M. and Neelin13, J.D., 2023. Diurnal Cycle of Precipitation Over
481 the Tropics and Central US: GCM Intercomparison. Quarterly Journal of the Royal
482 Meteorological Society.
- 483 Tao, C., Zhang, Y., Tang, Q., Ma, H.Y., Ghate, V.P., Tang, S., Xie, S. and Santanello,
484 J.A., 2021. Land–Atmosphere coupling at the US Southern Great Plains: A

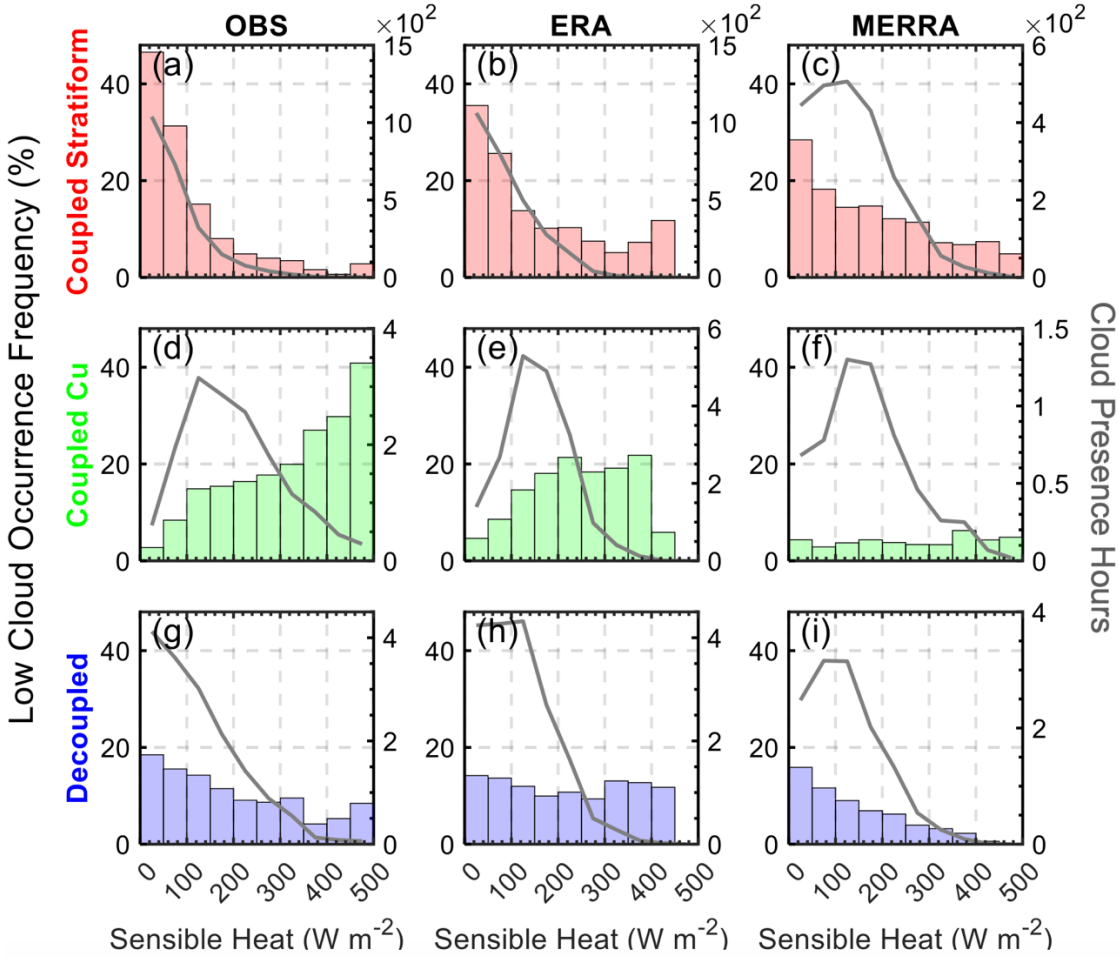
- 485 comparison on local convective regimes between ARM observations, reanalysis,
486 and climate model simulations. *Journal of Hydrometeorology*, 22(2), pp.463-481.
- 487 Tao, C., Zhang, Y., Tang, S., Tang, Q., Ma, H.Y., Xie, S. and Zhang, M., 2019. Regional
488 moisture budget and land-atmosphere coupling over the US Southern Great Plains
489 inferred from the ARM long-term observations. *Journal of Geophysical Research: Atmospheres*, 124(17-18), pp.10091-10108.
- 490 Teixeira, J., and Hogan, T. F. (2002): Boundary layer clouds in a global atmospheric
491 model: simple cloud cover parameterizations. *J. Climate*, 15(11), 1261–1276.
- 492 Tian, J., Zhang, Y., Klein, S.A., Öktem, R. and Wang, L., 2022. How does land cover
493 and its heterogeneity length scales affect the formation of summertime shallow
494 cumulus clouds in observations from the US Southern Great Plains?. *Geophysical
495 Research Letters*, 49(7), p.e2021GL097070.
- 496 Tiedtke, M. (1993). Representation of clouds in large-scale models. *Monthly Weather
497 Review*, 121(11), 3040-3061.
- 498 Tiedtke, M., 1993. Representation of clouds in large-scale models. *Monthly Weather
Review*, 121(11), pp.3040-3061.
- 499 Wang, Y., Hu, J., Li, R., Song, B., Hailemariam, M., Fu, Y. and Duan, J., 2023.
500 Increasing cloud coverage deteriorates evapotranspiration estimating accuracy from
501 satellite, reanalysis and land surface models over East Asia. *Geophysical Research
502 Letters*, 50(8), p.e2022GL102706.
- 503 Xian, T., Guo, J., Zhao, R., Su, T. and Li, Z., 2023. The impact of urbanization on
504 mesoscale convective systems in the Yangtze River Delta region of China: insights
505 gained from observations and modeling. *Journal of Geophysical Research: Atmospheres*, 128(3), p.e2022JD037709.
- 506 Xiao, H., Berg, L.K. and Huang, M. (2018). The impact of surface heterogeneities and
507 land-atmosphere interactions on shallow clouds over ARM SGP site. *Journal of
508 Advances in Modeling Earth Systems*, 10(6), pp.1220-1244.
- 509 Xie, S., McCoy, R.B., Klein, S.A., Cederwall, R.T., Wiscombe, W.J., Clothiaux, E.E.,
510 Gaustad, K.L., Golaz, J.C., Hall, S.D., Jensen, M.P. and Johnson, K.L., 2010.
511 Clouds and more: ARM climate modeling best estimate data: A new data product
512 for climate studies. *Bulletin of the American Meteorological Society*, 91(LLNL-
513 JRNL-412676).
- 514 Yang, Y.J., Wang, H., Chen, F., Zheng, X., Fu, Y. and Zhou, S., 2019. TRMM-based
515 optical and microphysical features of precipitating clouds in summer over the
516 Yangtze–Huaihe River valley, China. *Pure and Applied Geophysics*, 176, pp.357-
517 370.
- 518 Yue, Q., Kahn, B.H., Fetzer, E.J., Wong, S., Frey, R. and Meyer, K.G., 2017. On the
519 response of MODIS cloud coverage to global mean surface air temperature. *Journal
520 of Geophysical Research: Atmospheres*, 122(2), pp.966-979.

- 524 Zhang, M., Wang, X., Chen, J., Cheng, T., Wang, T., Yang, X., Gong, Y., Geng, F. and
525 Chen, C. (2010). Physical characterization of aerosol particles during the Chinese
526 New Year's firework events. *Atmospheric Environment*, 44(39), pp.5191-5198.
- 527 Zhang, Y. and Klein, S.A. (2010). Mechanisms affecting the transition from shallow to
528 deep convection over land: Inferences from observations of the diurnal cycle
529 collected at the ARM Southern Great Plains site. *Journal of the Atmospheric*
530 *Sciences*, 67(9), pp.2943-2959.
- 531 Zhang, Y. and Klein, S.A., 2013. Factors controlling the vertical extent of fair-weather
532 shallow cumulus clouds over land: Investigation of diurnal-cycle observations
533 collected at the ARM Southern Great Plains site. *Journal of the Atmospheric*
534 *Sciences*, 70(4), pp.1297-1315.
- 535 Zhang, Y., Klein, S.A., Fan, J., Chandra, A.S., Kollas, P., Xie, S. and Tang, S., 2017.
536 Large-eddy simulation of shallow cumulus over land: A composite case based on
537 ARM long-term observations at its Southern Great Plains site. *Journal of the*
538 *Atmospheric Sciences*, 74(10), pp.3229-3251.
- 539 Zheng, Y., Zhang, H., Rosenfeld, D., Lee, S.S., Su, T. and Li, Z. (2021). Idealized large-
540 eddy simulations of stratocumulus advecting over cold water. Part I: Boundary layer
541 decoupling. *Journal of the Atmospheric Sciences*, 78(12), pp.4089-4102.

542 **Figures**

543

544 **Figure 1.** Comparison of observations and reanalysis for the relationships between low
 545 clouds and surface fluxes. Histograms represent the average frequency of low cloud
 546 occurrences binned by surface sensible heat (a, c, e) and latent heat flux (b, d, f) during
 547 09:00-15:00 LT. Red lines indicate the number of hours with low cloud occurrence
 548 within each flux bin. Cases with precipitation exceeding 0.1mm h^{-1} are excluded from
 549 analyses. The first (a, b), second (c, d), and third rows (e, f) correspond to observations,
 550 ERA-5, and MERRA-2 respectively.

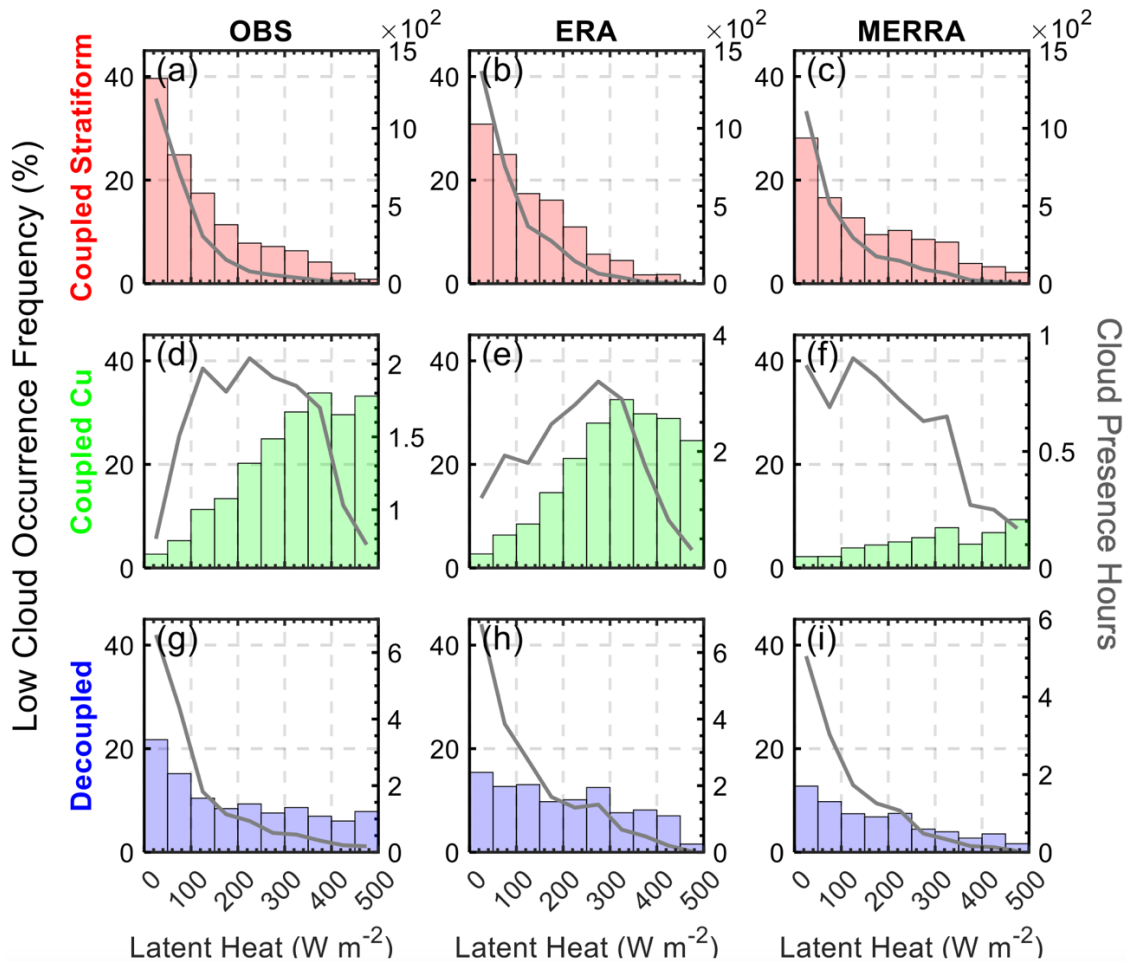


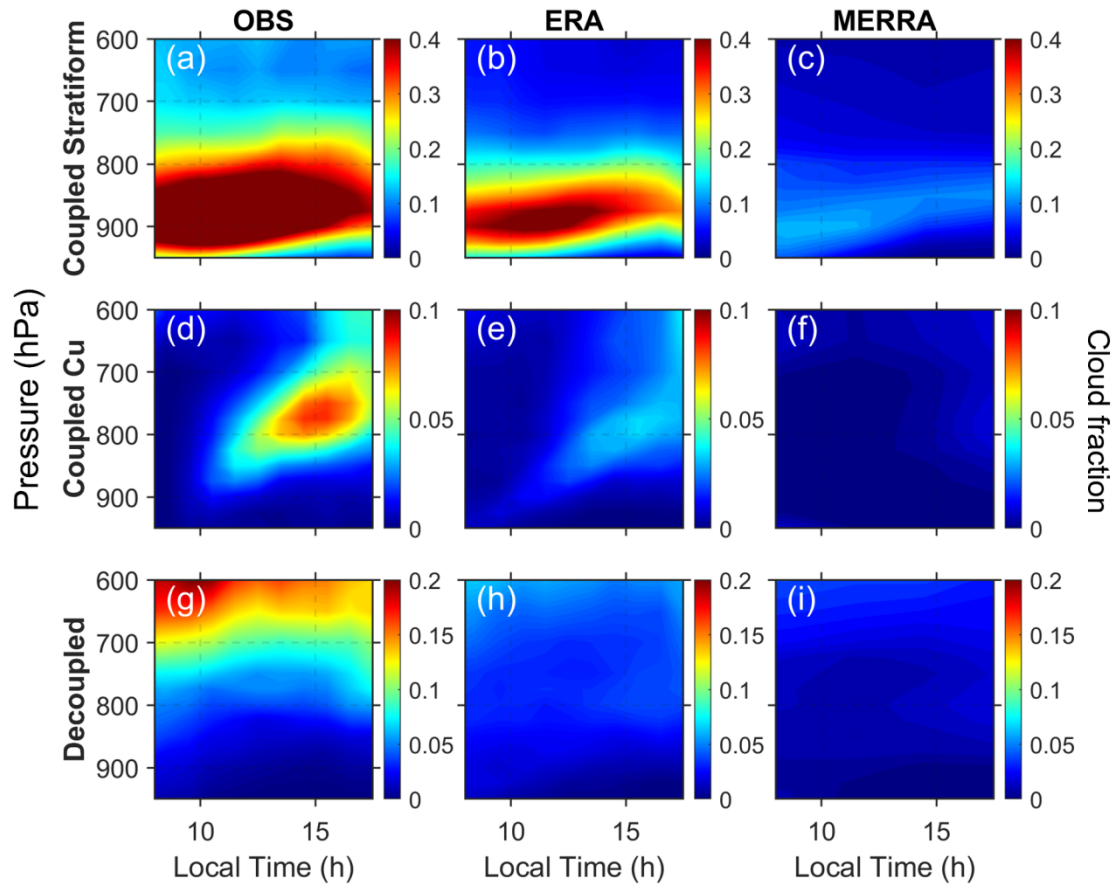
551

552 **Figure 2.** Cloud occurrence frequency and surface sensible heat relationships
 553 segregated by conditions of cloud regimes during 09:00-15:00 LT. The histograms
 554 display the average frequency of different cloud types binned by surface sensible heat
 555 flux for observational (OBS), ERA reanalysis, and MERRA reanalysis datasets. Panels
 556 (a) to (c) showcase coupled stratiform clouds, panels (d) to (f) depict coupled cumulus
 557 clouds, and panels (g) to (i) present decoupled clouds. Grey lines indicate the number
 558 of hours with low cloud occurrence within each flux bin.

559

560

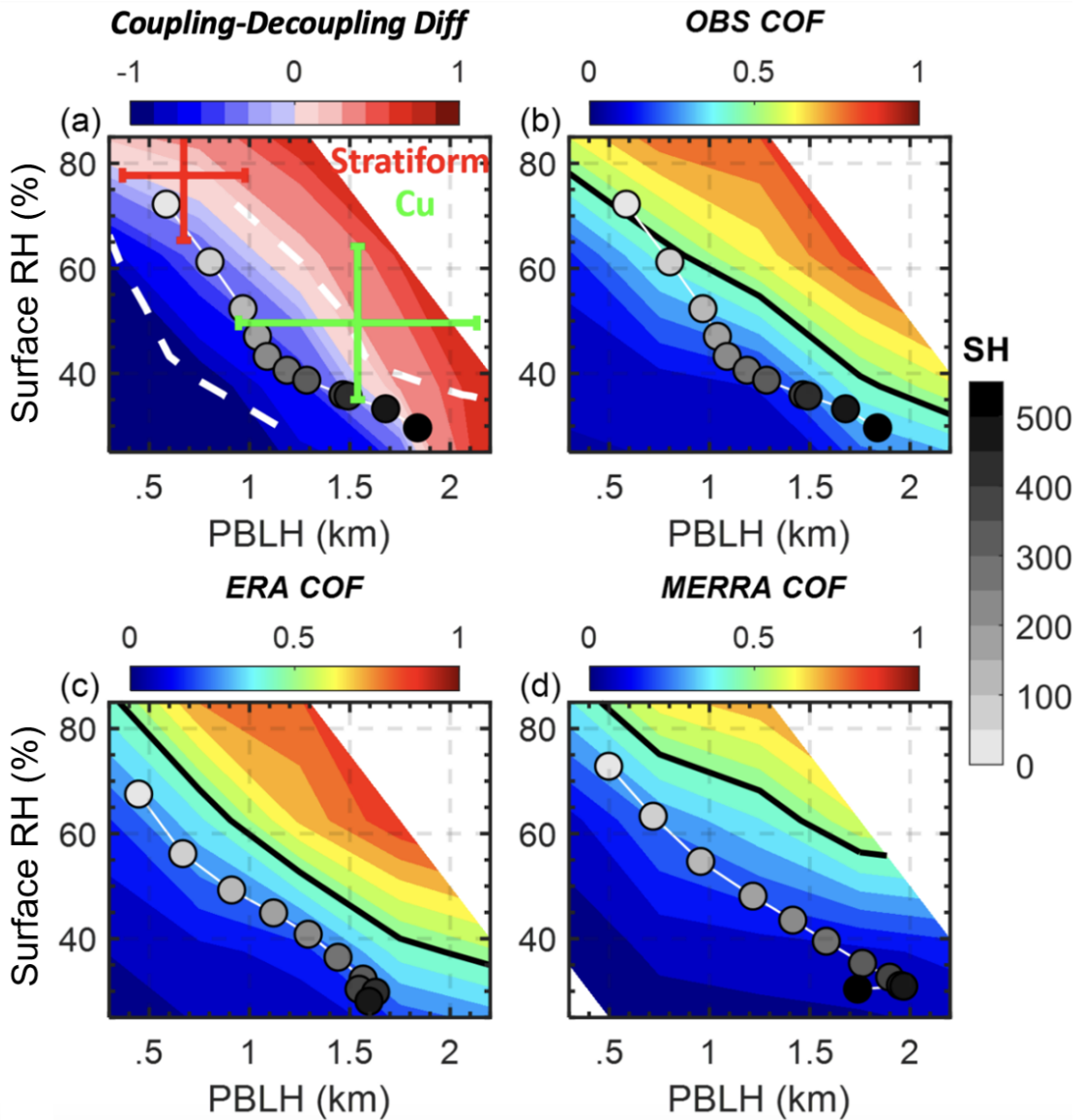




565

566 **Figure 4.** Diurnal variation of cloud fraction with atmospheric pressure across different
 567 cloud regimes in observations and reanalysis data. This figure presents contour plots
 568 that display the variation of cloud fraction during the daytime at various atmospheric
 569 pressures for three distinct scenarios: coupled stratiform clouds, coupled cumulus, and
 570 decoupled clouds. Each row represents one of the cloud scenarios, with observational
 571 data (OBS) in the first column, ERA reanalysis data in the second column, and MERRA
 572 reanalysis data in the third column.

573



574
 575 **Figure 5.** (a) The values of the coupling-decoupling difference (the frequency of
 576 coupled clouds minus the frequency of decoupled clouds) vary under the different
 577 ranges of Planetary Boundary Layer Height (PBLH) and surface relative humidity
 578 (RH_{sfc}). (b-d) The values of the low cloud occurrence frequency (COF) correspond to
 579 PBLH and RH_{sfc} from (b) observations, (c) ERA-5, and (d) MERRA-2. In (a), the means
 580 and standard deviations of stratiform clouds and cumulus are marked. The grey-scale
 581 dots indicate the averages of PBLH and RH_{sfc} for different sensible heat values. The
 582 dash white lines in (a) indicate the range of standard deviations of different PBLH for
 583 different sensible heat bins. The black line denoting the position of 50% COF.

584

585

586

587



PUBLICATIONS

588

Supporting Information for

590 **Observation and Reanalysis Derived Relationships Between Cloud and Land**
591 **Surface Fluxes Across Cumulus and Stratiform Coupling Over the Southern**
592 **Great Plains**

593

594 Tianning Su^{1,2}, Zhanqing Li¹, Yunyan Zhang², Youtong Zheng^{3,4}, Haipeng Zhang¹

595

⁵⁹⁶ ¹AOSC & ESSIC, University of Maryland at College Park, Maryland, 20740, USA

²Lawrence Livermore National Laboratory, Livermore, CA, USA

³Department of Earth and Atmospheric Science, University of Houston, Houston, TX,
USA

602

⁶⁰³ *Corresponding authors: zhanqing@umd.edu; su10@llnl.gov

604

605 **Contents of this file**

606 This PDF file includes:

607

608

Text S1

609 Figs. S1 to S9

611 **S. 1 Descriptions of datasets:**

612 **(1) Thermodynamic profiles from radiosonde**

613 We will use radiosonde measurements to characterize the thermodynamic settings
614 of the PBL. Radiosondes are routinely launched multiple times at the ARM sites.
615 Holdridge et al. (2011) provided technical details about the ARM radiosonde. Using the
616 well-established method developed by Liu and Liang (2010), we retrieved PBLHs over
617 the SGP site based on the vertical profiles of potential temperature from radiosonde
618 measurements.

619 **(2) Active Remote Sensing of Clouds (ARSCL)**

620 We will use the well-established ARM cloud product, named ARSCL, generated for
621 each ARM site (Clothiaux et al., 2000; Flynn et al., 2017). ARSCL provides the vertical
622 boundaries of clouds by combining data from the MPL, ceilometer, and cloud radar,
623 conveying useful information pertaining to the vertical structure and temporal evolution
624 of clouds (Kollias et al., 2007). For the lowest cloud base, we will use the best
625 estimation from laser-based techniques (i.e., MPL and ceilometer). Based on ARSCL,
626 Xie et al. (2010) offers a comprehensive dataset of cloud fraction profiles.

627 **(3) Surface fluxes**

628 Surface fluxes are critical for PBL development and closely interact with low clouds
629 as the driving force. A value-added product at ARM called the bulk aerodynamic latent
630 and sensible heat fluxes from energy balance Bowen ratio (BAEBBR) was generated
631 to replace energy balance Bowen ratio flux measurements with a bulk aerodynamic
632 estimation when the Bowen Ratio (Wesely et al., 1995). We use the Best Estimate

633 Sensible/Latent Heat Fluxes in the BAEBBR product.

634 **(4) ARMBE2DGRID**

635 The ARMBE2DGRID VAP provides a dataset by integrating key surface
636 measurements from the Southern Great Plains sites, consolidating them into a uniform
637 2D grid (<https://www.arm.gov/capabilities/science-data-products/vaps/armbe2dgrid>).

638 The dataset delivers hourly data with a spatial resolution of $0.25^{\circ} \times 0.25^{\circ}$. It
639 encompasses a wide range of products including Surface Meteorological
640 Instrumentation, data from Oklahoma Mesonet and Kansas State University Mesonet,
641 Quality Controlled Radiation Data, observations from Geostationary Operational
642 Environmental Satellites, Microwave Radiometer, Best-Estimate Fluxes from
643 BAEBBR, ECOR outputs, and Soil Water and Temperature System data. Rigorous
644 Quality Controls are employed to ensure the reliability of the data.

645 **(5) MODIS aboard the NASA Aqua and Terra**

646 NASA's Aqua and Terra satellites, carrying the Moderate Resolution Imaging
647 Spectroradiometer (MODIS), provides high-quality data on global cloud coverage. The
648 corrected reflectance product from MODIS offers a true-color view of the Earth's
649 surface and atmosphere, allowing for accurate confirmation of cloud presence and
650 extent (Schaaf et al., 2002). By analyzing the true-color imagery, we can inspect cloud
651 regimes, checking stratiform and cumulus for coupled clouds. NASA MODIS
652 imageries are achieved in <https://worldview.earthdata.nasa.gov/>.

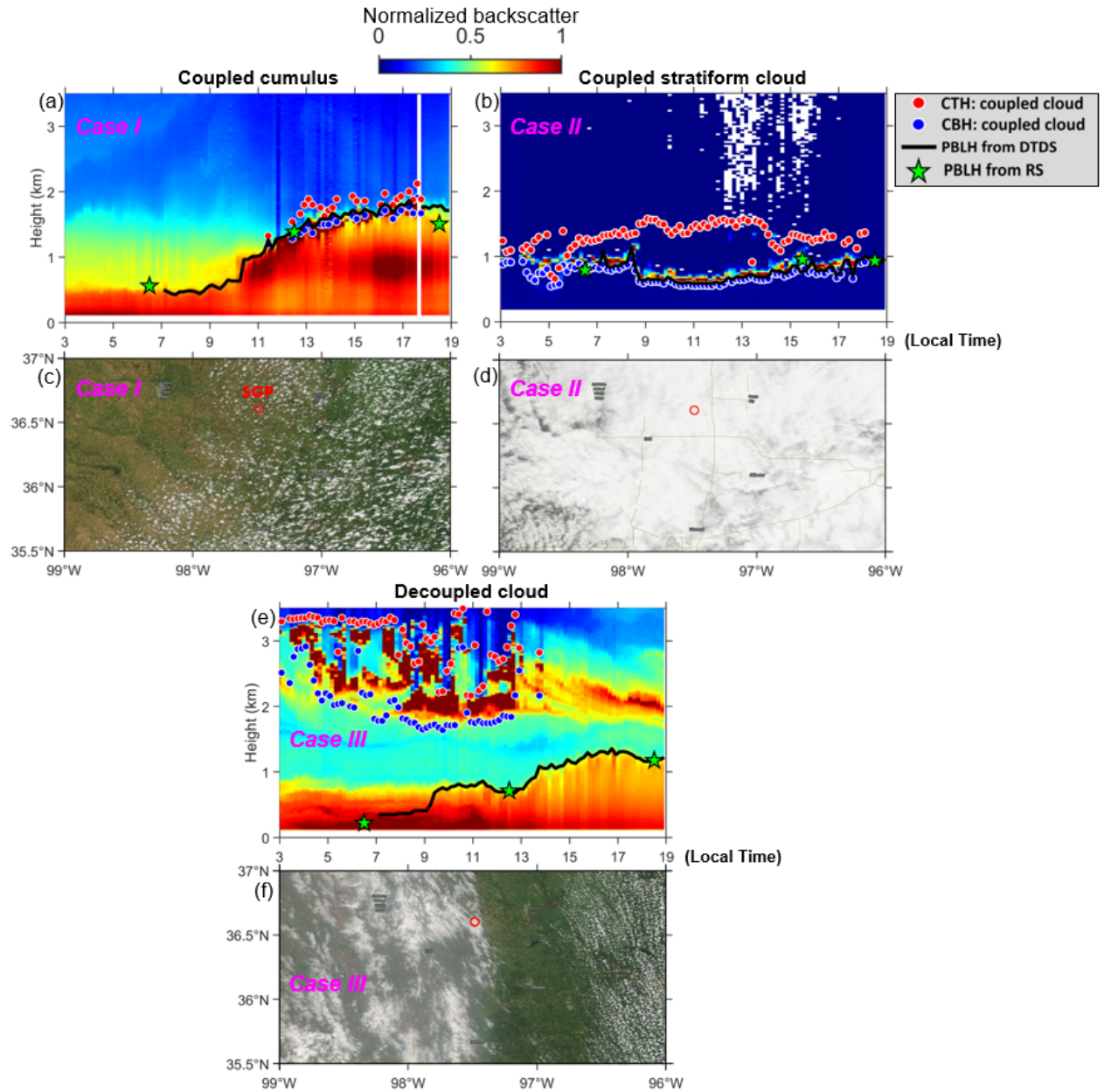
653 **(6) ERA-5 Reanalysis Data**

654 As one of the most advanced and widely used reanalysis data, ERA-5, produced

655 by the European Centre for Medium-Range Weather Forecasts (ECMWF), provides a
656 high-resolution, hourly updated global atmospheric reconstruction (Hersbach et al.
657 2020). Utilizing advanced assimilation of vast amounts of observational data, ERA-5
658 offers comprehensive climate variables, including temperature, humidity, wind, and
659 cloud properties. We used this dataset to compare cloud-land relationships between
660 observation and reanalysis datasets. With its fine spatial resolution and temporal
661 coverage, ERA-5 allows for analysis of cloud formation, relating to PBL
662 thermodynamics and surface processes.

663 **(7) MERRA-2 Reanalysis Data**

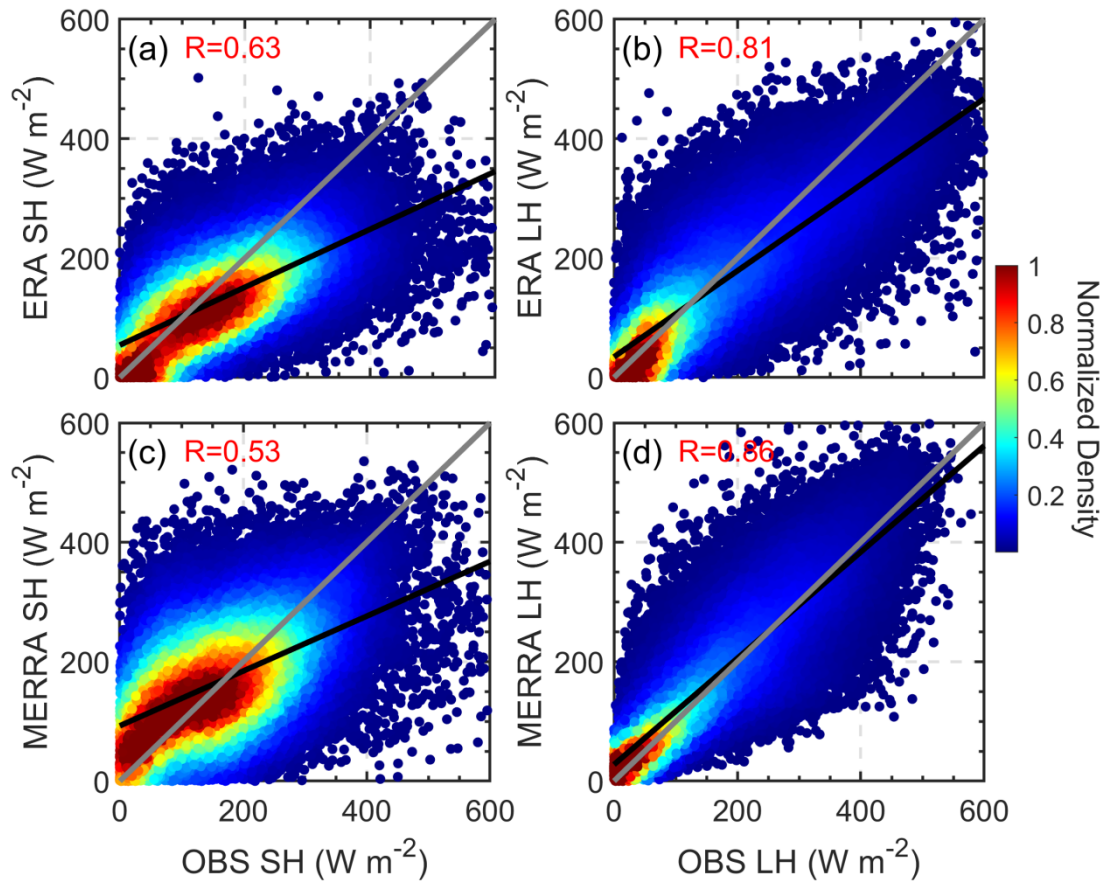
664 The Modern-Era Retrospective analysis for Research and Applications, Version
665 2 (MERRA-2), developed by NASA, is an improved reanalysis dataset focusing on the
666 representation of the hydrological cycle, aerosols, and atmospheric composition
667 (Gelaro et al., 2017). MERRA-2 integrates satellite and ground-based observational
668 data to provide a coherent record of the global atmosphere. The low cloud fraction data
669 are provided at a temporal resolution of one hour, while the vertical cloud fraction are
670 available at three-hour intervals. In this study, MERRA-2's extensive coverage and
671 detailed depiction of atmospheric variables are used to examine the cloud occurrences
672 and their relationship with surface fluxes.

673 **Figures**

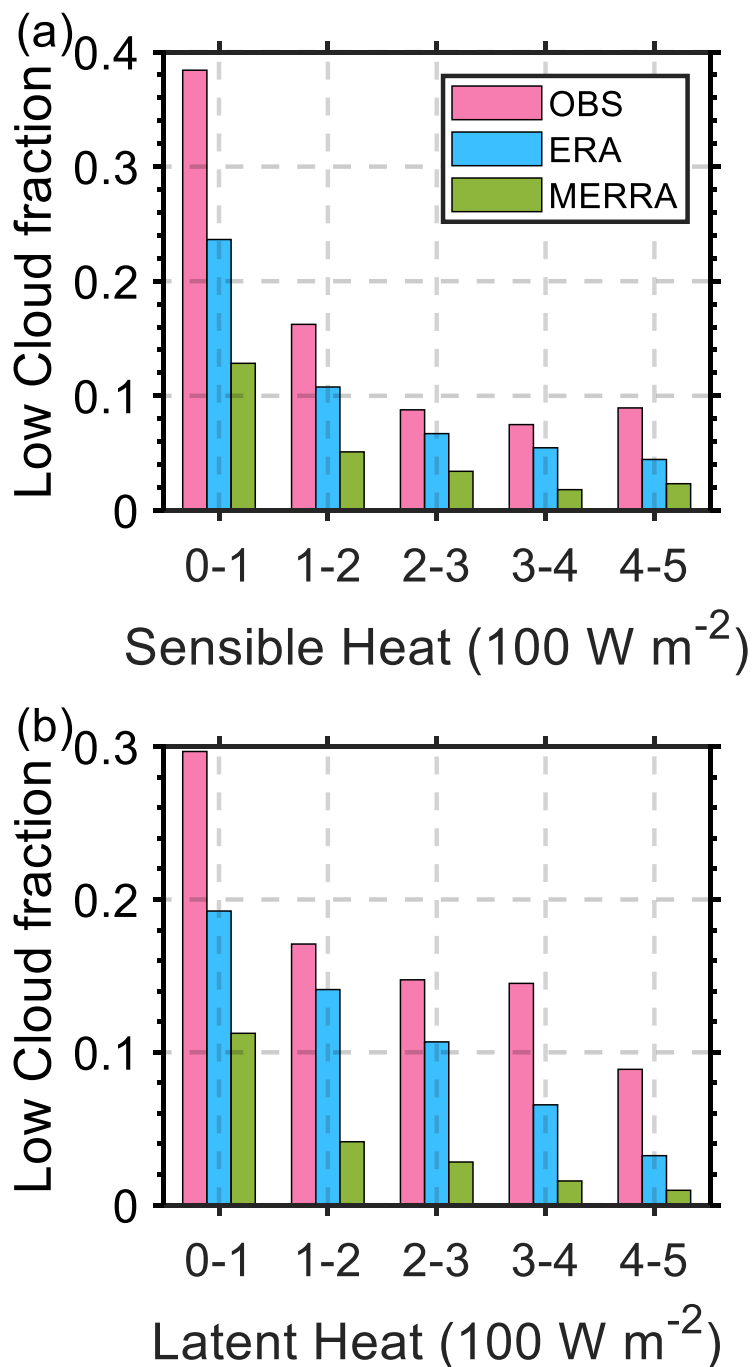
674

675 **Figure S1.** Daily vertical profiles of backscatters for coupled cumulus (a, Case I) and
 676 coupled stratiform cloud (b, Case II). Backscatter is normalized to a range of 0-1, in
 677 arbitrary units. Red dots and blue dots indicate the CTH and CBH of coupled cloud.
 678 Black lines and green stars mark the PBLH retrieved from MPL and radiosonde. (c and
 679 d) 2-D view of the corrected reflectance (true color) derived from MODIS (Aqua) for
 680 Case I (c) and Case II (d). The red circle marks the position of SGP site. (e-f) Daily

681 vertical profiles of backscatters and the satellite image for decoupled cloud (Case III).



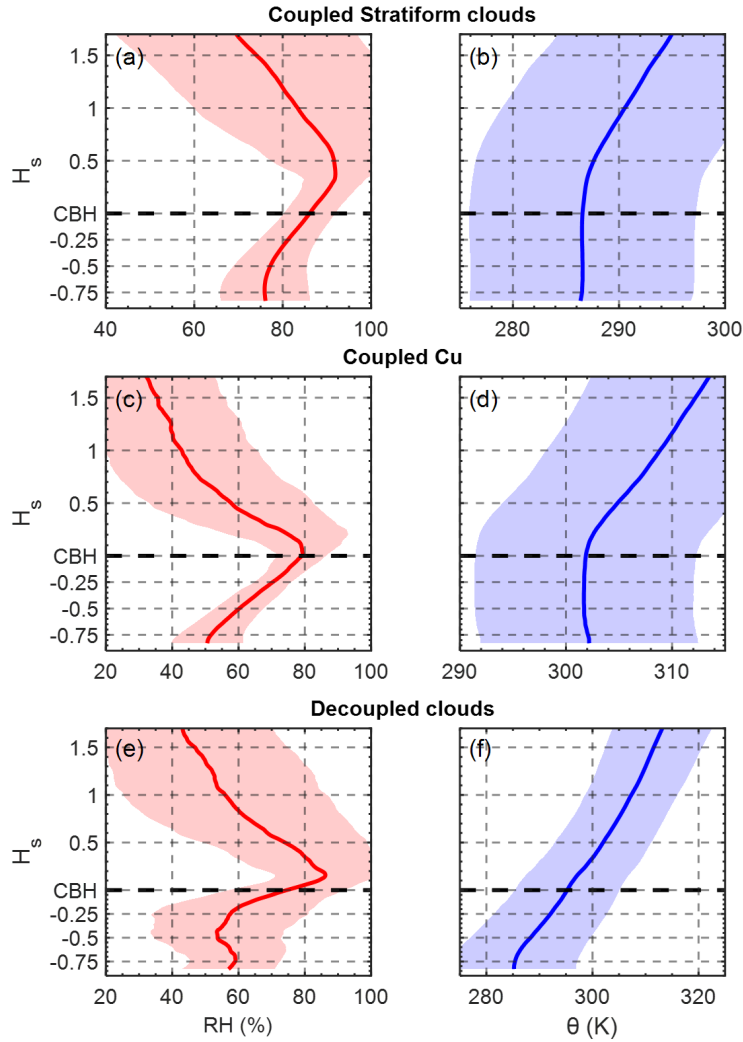
693



694

695 **Figure S3.** Comparison of average low cloud fraction across varying ranges of sensible
696 and latent heat fluxes. The low cloud fraction is defined as the maximum cloud fraction
697 occurring between the surface and 700 hPa. The data are categorized by source, with

698 observations (OBS), ERA-5, and MERRA-2 depicted in pink, blue, and green bars,
699 respectively.



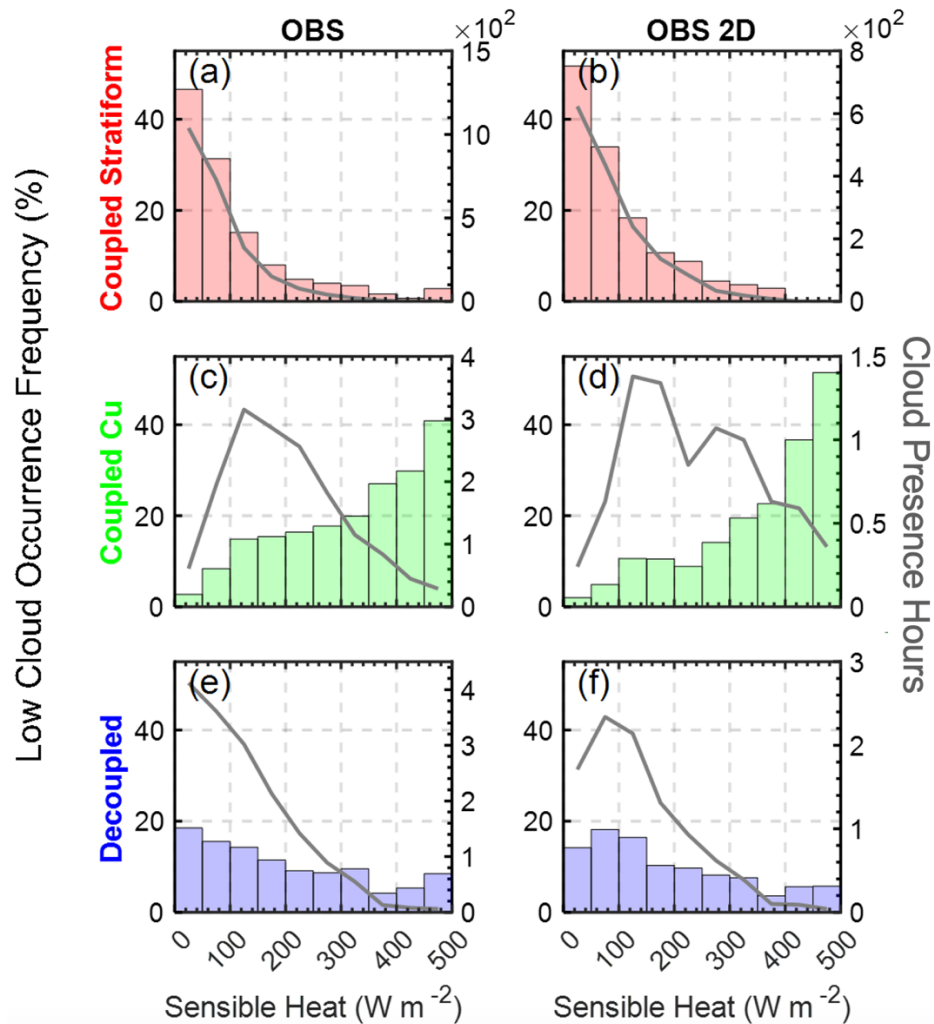
700 **Figure S4.** The average profiles of RH (red line) and virtual potential temperature (θ_v ,
701 blue line) for (a) coupled stratiform cloud, (b) coupled cumulus, and (c) decoupled
702 cloud. The vertical scale is normalized by CBH (black dash line). The red and blue
703 shaded areas indicate the standard deviations for RH and virtual potential temperature,
704 respectively.
705

706

707

708

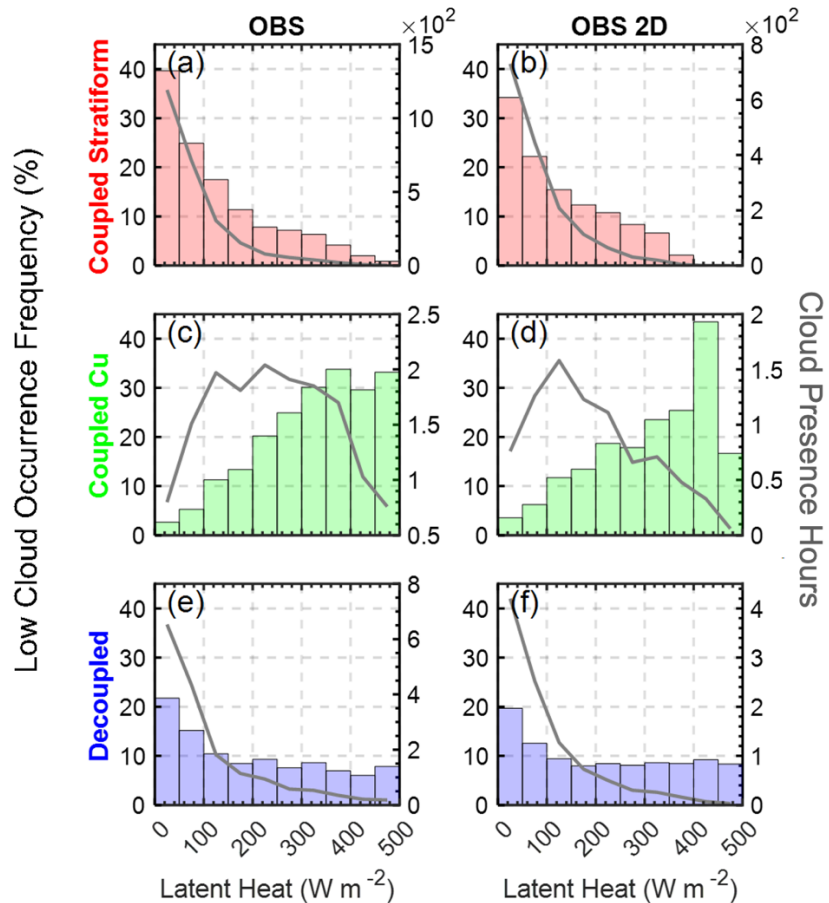
709



710

711 **Figure S5.** Cloud occurrence frequency and surface sensible heat relationships
 712 segregated by conditions of cloud regimes during 09:00-15:00 LT. The histograms
 713 display the average frequency of different cloud types binned by surface sensible heat
 714 flux for point observation (OBS) from the BAEBBR and for the 2D observation (OBS
 715 2D) from the ARM BE2DGRID. Grey lines indicate the number of hours with low cloud
 716 occurrence within each flux bin.

717



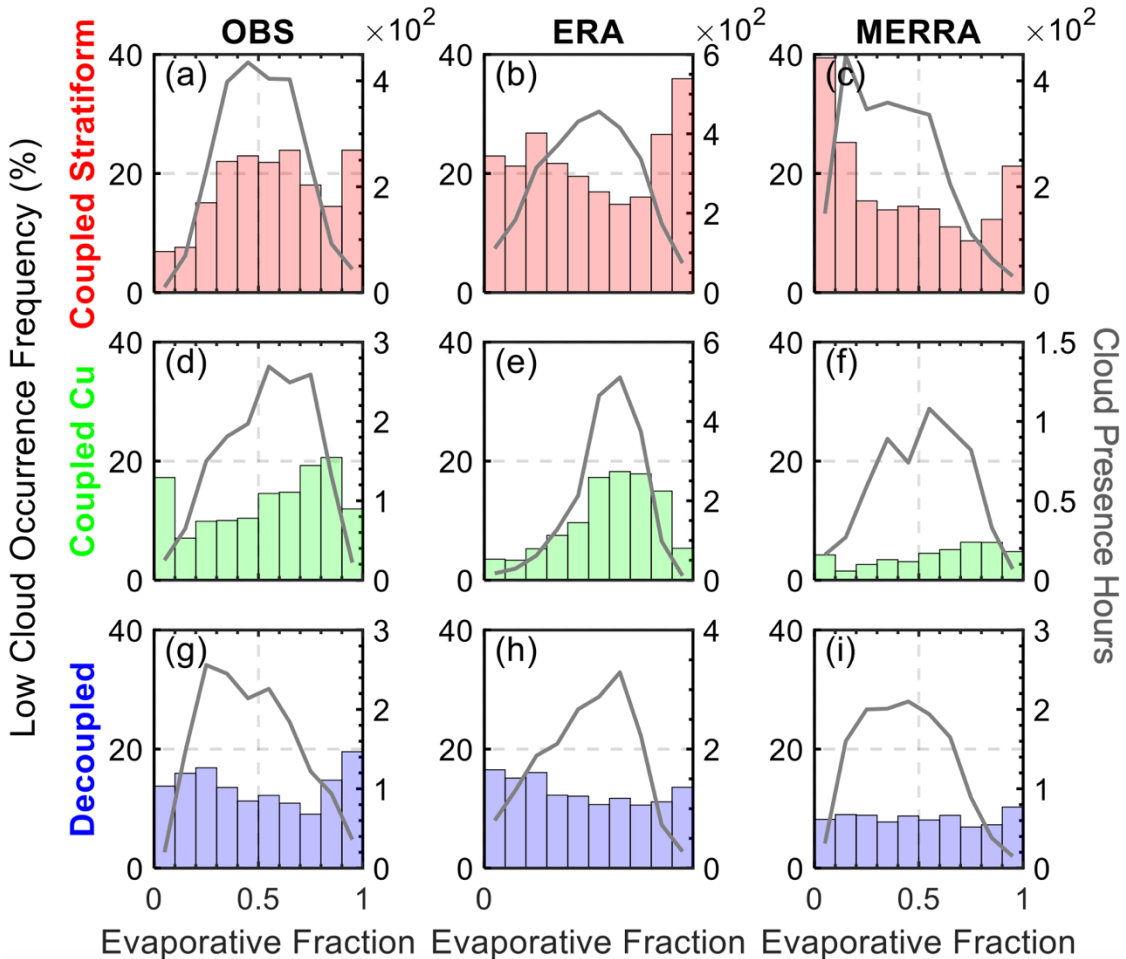
718

719 **Figure S6.** Similar to Figure S5, but depicting the relationships between low cloud
720 occurrence frequency and surface latent heat fluxes.

721

722

723



724

725 **Figure S7.** Similar to Figure S5, but depicting the relationships between low cloud
 726 occurrence frequency and evaporative fraction. Evaporative fraction is calculated as

$$727 \quad \frac{\text{Latent Heat}}{\text{Latent Heat} + \text{Sensible Heat}}.$$

728

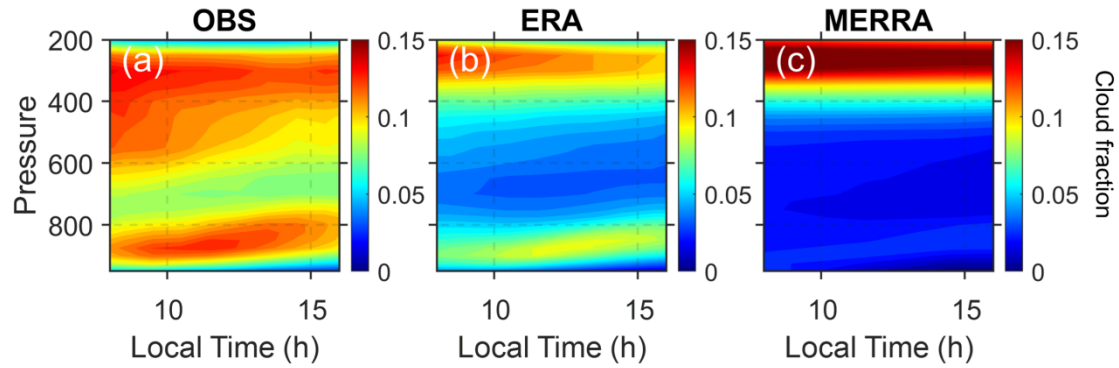
729

730

731

732

733



734

735 **Figure S8.** Diurnal Variation of Cloud Fraction in Observations and Reanalysis Data.

736 Contour plots represent the diurnal cycle of cloud fraction as a function of pressure (in
 737 hPa) for observational (OBS, a) and two reanalysis datasets (ERA and MERRA, b-c).

738

739

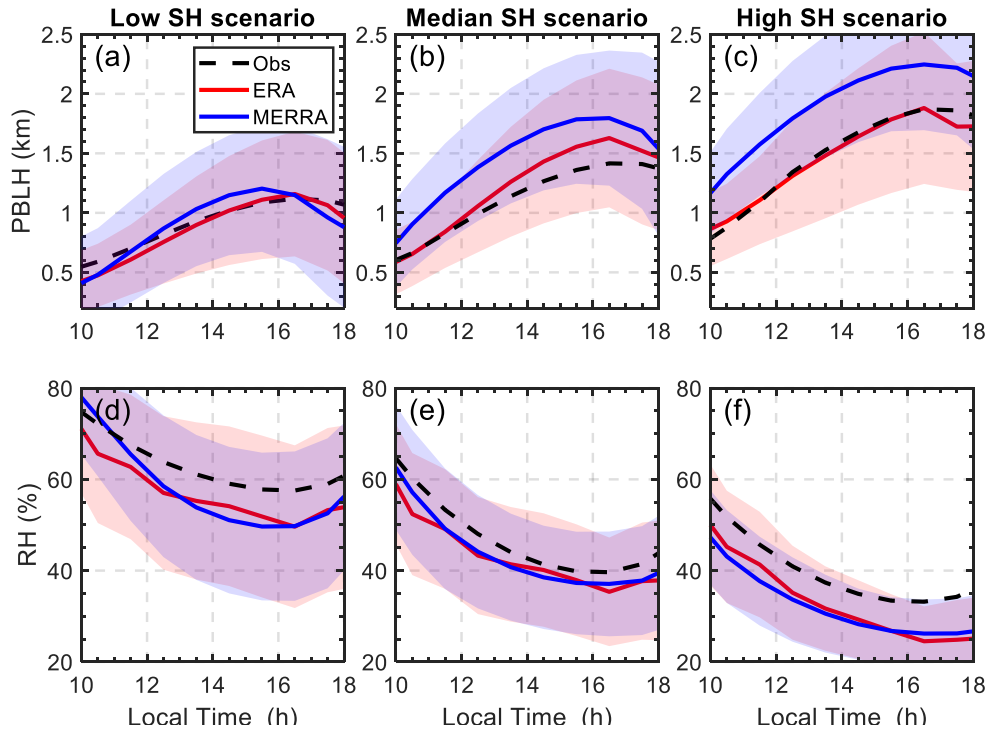
740

741

742

743

744



745

746 **Figure S9.** Diurnal variations in PBLH and RH across different sensible heat (SH)

747 scenarios. The graphs illustrate the progression of PBLH and RH throughout the day,

748 segmented into three sensible heat categories: low (0-200) (a, d), median (200-400) (b,

749 e), and high ($>400 \text{ W m}^{-2}$) (c, f). Solid lines represent the mean values from

750 observations (Obs), ERA-5 reanalysis (ERA), and MERRA-2 reanalysis (MERRA).

751 Shaded areas indicate one standard deviation from the mean, providing a visual

752 representation of variability within each dataset.

753

754

755

756

757

758

759 **References**

- 760 Clothiaux, E. E., Ackerman, T. P., Mace, G. G., Moran, K. P., Marchand, R. T., Miller,
761 M. A., & Martner, B. E. (2000). Objective determination of cloud heights and radar
762 reflectivities using a combination of active remote sensors at the ARM CART sites.
763 Journal of Applied Meteorology, 39(5), 645-665.
- 764 Flynn, D., Shi, Y., Lim, K., & Riihimaki, L. (2017). Cloud Type Classification (cldtype)
765 Value-Added Product. Ed. by Robert Stafford, ARM Research Facility. DOE/SC-
766 ARM-TR-200.
- 767 Gelaro, R., McCarty, W., Suárez, M.J., Todling, R., Molod, A., Takacs, L., Randles,
768 C.A., Darmenov, A., Bosilovich, M.G., Reichle, R. and Wargan, K., 2017. The
769 modern-era retrospective analysis for research and applications, version 2
770 (MERRA-2). Journal of climate, 30(14), pp.5419-5454.
- 771 Hersbach, H., Bell, B., Berrisford, P., Hirahara, S., Horányi, A., Muñoz-Sabater, J.,
772 Nicolas, J., Peubey, C., Radu, R., Schepers, D. and Simmons, A., 2020. The ERA5
773 global reanalysis. Quarterly Journal of the Royal Meteorological Society, 146(730),
774 pp.1999-2049.
- 775 Holdridge, D., Ritsche, M., Prell, J., and Coulter, R. (2011): Balloon-borne sounding
776 system (SONDE) handbook, <https://www.arm.gov/capabilities/instruments/sonde>.
- 777 Kollias, P., Clothiaux, E. E., Miller, M. A., Albrecht, B. A., Stephens, G. L., &
778 Ackerman, T. P. (2007). Millimeter-wavelength radars: New frontier in atmospheric
779 cloud and precipitation research. Bulletin of the American Meteorological Society,
780 88(10), 1608-1624.

- 781 Liu, S., & Liang, X. Z. (2010). Observed diurnal cycle climatology of planetary
782 boundary layer height. *Journal of Climate*, 23(21), 5790-5809.
- 783 Schaaf, C.B., Gao, F., Strahler, A.H., Lucht, W., Li, X., Tsang, T., Strugnell, N.C., Zhang,
784 X., Jin, Y., Muller, J.P. and Lewis, P., 2002. First operational BRDF, albedo nadir
785 reflectance products from MODIS. *Remote sensing of Environment*, 83(1-2),
786 pp.135-148.
- 787 Wesely, M. L., Cook, D. R., and Coulter, R. L. (1995): Surface heat flux data from
788 energy balance Bowen ratio systems (No. ANL/ER/CP-84065; CONF-9503104-2).
789 Argonne National Lab., IL (United States).
- 790 Xie, S., McCoy, R.B., Klein, S.A., Cederwall, R.T., Wiscombe, W.J., Clothiaux, E.E.,
791 Gaustad, K.L., Golaz, J.C., Hall, S.D., Jensen, M.P. and Johnson, K.L., 2010.
792 Clouds and more: ARM climate modeling best estimate data: A new data product
793 for climate studies. *Bulletin of the American Meteorological Society*, 91(LLNL-
794 JRNL-412676).